ELSEVIER

Land-based remote sensing of snow for the validation of a snow transport model

Javier G. Corripio*, Yves Durand, Gilbert Guyomarc'h, Laurent Mérindol,
Dominique Lecorps, Philippe Pugliése

Centre d'Etudes de la Neige, Météo France-CNRM 1441, Rue de la Piscine F-38406 St. Martin d'Heres-Cedex, France

Abstract

As part of the effort of the Centre d'Etudes de la Neige (CEN), Météo France, for the improvement in modelling snow cover evolution and avalanche risk forecasting, a numerical simulation of snow transport and related mechanical effects on snow particles morphology has been developed during the last years. The objective is to incorporate the wind effects into the Météo France operational chain SAFRAN–CROCUS–MEPRA for avalanche risk forecasting. At present, an evaluation version of the model is applied to a well-instrumented site (Col du Lac Blanc 2700 m, French Alps), in order to assess its performance and validate its applicability. Here, in addition to nivo-meteorological stations, several specific snowdrift sensors and a range of snow depth poles, a novel remote sensing technique based on terrestrial photography is being applied. Oblique digital photographs of the area are taken periodically and after snowdrift events from an elevated viewpoint. These photographs are then georeferenced to a digital elevation model (DEM). Further radiometric corrections depending on topography and atmospheric conditions are applied to the georeferenced pixels to derive relative albedo. Spectral filtering applied to the digital camera permits detecting small variations in the associated snow grain characteristics. The effects of wind transport, erosion, accumulation and snow grain characteristics described by the model can then be monitored by measuring the associated changes in albedo, slope angles, texture and texture orientation and feature variations recorded by the photographs. This new tool seems to be an appropriate technique for spatial validation of snowdrift modelling, and it is useful in identifying both the strengths and weaknesses of the model. The results for the ongoing campaign on the 2002–2003 winter will be presented and discussed.
© 2004 Elsevier B.V. All rights reserved.

Keywords: Snowdrift; Photography; Georeferencing; Albedo; DEM; Spatial validation

1. Introduction

Snow wind transport has an important effect on the spatial distribution of the snow pack, which in turn is important to assess snow stability, due to both redistribution of load and changes in the shape of snow grains and crystals due to collisions during transport. Additionally, this redistribution of mass has effects on

---
* Corresponding author. Present address: Swiss Federal Institute of Technology, IHW-ETH, Wolfgang Pauli Strasse 15, Honggerberg HIL g 28.1, CH-8093 Zurich, Switzerland. Tel.: +41-1-6334965; fax: +41-1-6331061.

E-mail address: Javier.Corripio@ethz.ch (J.G. Corripio).

glacier mass balance, hydrological resources derived from snow and local microclimates; it also has small-scale ecological implications (Pomeroy and Gray, 1995). The correct avalanche risk estimation requires accurate knowledge of snow and temperature profiles, types of snow grain, density, strength and cohesion (Mellor, 1965; Föhn and Meister, 1983; Takeuchi, 1980). However, a modelling tool for the estimation of these parameters should incorporate not only the snow from direct precipitation but also that being added by wind transport. This is not an easy task, especially in mountainous terrain, where the small-scale topography plays an important role (e.g., in the formation of cornices, sastruguis, slabs). Furthermore, any modelling attempt should be fast and accurate enough to be used as an aid tool in real-time, realistic, avalanche hazard estimation.

For about 10 years, the Centre d'Etudes de la Neige (CEN), Météo France, has developed different models of snow wind transport in increasing degrees of complexity. At present, the current model under evaluation, SYTRON2, estimates snowdrift at a fine horizontal scale (about 1 km of characteristic length on a grid cell size of about 50 m) and incorporates the real topography as derived from a digital elevation model (DEM). It is run for a test site at the Col du Lac Blanc, Massif des Rousses, French Alps, where two nivo-meteorological stations, several specific snow drift sensors and a range of snow depth poles measure snow depth variations at several points. A realistic validation of this model demands a step forward from the traditional methods of point measurements toward a fully spatial evaluation of the results. However, this poses additional complications in terms of designing tools that are practical both in terms of cost and implementation. The magnitude of transported snow in a snowdrift event is of the order of cm when averaged over the whole surface of a grid cell (2500 m^2). This change can be measured precisely at a few points, but it is too small to permit a direct measurement over medium or large areas. Thus, an alternative approach is followed. Here we explore the potential of oblique land-based photography as a remote sensing tool for the validation of the model. These photographs are then georeferenced to a digital elevation model and analysed using different techniques of image processing applied to remote sensing. The main pur-

pose of this tool is identifying areas of snow erosion and deposition that can be compared to the output of the model.

2. Snowdrift modelling

Snowdrift modelling is a difficult challenging task due to different factors such as the large range of the working scales (from the synoptic to the micro-topographical scale) and the permanent interaction between local topography, meteorological conditions and the snow. Nevertheless, these phenomena cannot be neglected in the framework of an automatic system of snow modelling and avalanche hazard forecasting. Several valuable attempts have been successfully done by several workers (Gauer, 1998; Liston and Sturm, 1998; Lehning et al., 2002). Our present version runs at a scale of about 400 km^2 and provides only the large-scale conditions for wind and snow (Durand et al., 1999). Current research work aims at the operational incorporation of a high-resolution model at a fine mesh size of about 50 m, which coupled with the lower resolution, but a higher spatial extent model allows the realistic modelling of snowdrift effects. Presently this last model, called SYTRON2, is at the testing and validation stage.

SYTRON2 is initialised with a realistic snow pack information derived from the Météo France operational avalanche hazard estimation chain SAFRAN–CROCUS–MEPRA outputs, and coupled to a wind field computed by the new SAMVER model. This last model is a downscaling process from the massif scale, computed by SAFRAN (Durand et al., 1999), to the range 600 to 45 m. The model accounts for wind deflection due to local surface slope (Ryan, 1977; Purves et al., 1998), for variation of wind speed due to topographic slope and curvature, following an approach similar to that of Liston and Sturm (1998), and is based on the conservation of the potential vorticity and divergence on isentropic surfaces (Holton, 1979; Durand et al., in press). Once initialised with realistic wind and snow conditions from the model SAMVER, the 2D drifting model SYTRON2 is able to simulate the occurrence of blowing snow and to estimate the bulk snow mass exchanges due to creep, saltation and suspension. The losses by sublimation as well as the modifications of density and

crystal morphology are also treated (Durand et al., in press).

During transport, the characteristics of the snow crystals are modified both by mechanical interaction with other snow crystals and by partial sublimation. SYTRON2 algorithms tend to make the new drifted crystals closer to small rounded grains, a realistic situation during snowdrift. These transformations are a multistep process. The snow crystal characteristics are described using the parameters of the model CROCUS (Brun et al., 1992). A fresh snow crystal is thus defined in terms of dendricity (ranging from 1 to 0) and sphericity (0 to 1). When drifted, a snow crystal dendricity is made to decrease and its sphericity to increase according to the wind velocity. The operators governing crystal change are based on the laws of snow metamorphism used by CROCUS and additional observation of the drifted crystals, done at the instrumented site for many years (Guyomarc'h and Mérindol, 1991, 1995). At each grid point and time step, the deposited snow is then added to the snow bed by aggregation to the first layer or through a new layer if the amount is deep enough. A new snow profile is then made at each grid point, where density and snow grain characteristics (dendricity and sphericity) are recalculated. At this stage, SYTRON2 uses the original CROCUS temperature profile but does not recalculate it. A more complete thermodynamic treatment of the new snow profile will be incorporated in future versions of SYTRON2. Fresh snow, in case of snowfall, is simply added to the snow mass in movement and treated as if it were eroded snow. This allows a deposition of the fresh snow suited to the wind and topographic conditions. All these formulations have an implicit self limitation: the transported snow is less subject to a new drifting effect during the following hours because it underwent some crystal changes which decrease the corresponding snow-driftability index and thus the transportability.

3. Methodology

3.1. Georeferencing terrestrial photography

In order to monitor the changes in the snow pack, we take photographs of the study site from different viewpoints. As we are working on an Alpine site, it is relatively easy to find elevated points with good visibility over the area. The photographs are taken with a very good quality digital camera fitted with a CCD (Charge-Coupled Device) recording 6 million pixels. These photographs are then georeferenced to the digital elevation model using a procedure described by Corripio (in press) that follows standard procedures for perspective views in computer graphics (Fiume, 1989; Foley et al., 1990). To summarise, this technique consists of creating a "virtual" photography of the DEM that then can be scaled to the resolution of the photographic image to establish a mapping function between pixels in the photograph and grid cell points. This allows locating the exact position of pixels in the oblique image. The georeferencing process consists of a viewing transformation applied to the DEM in which the coordinates of every grid cell are firstly translated to refer them to a coordinate system with origin at the camera position. Then, a transformation is applied according to the viewing direction and focal length of the camera (Eq. (1)). This results in a three-dimensional set of points corresponding to the cells in the DEM as seen from the point of view of the camera. Finally, the resulting viewing transformation is projected into a two-dimensional viewing "window", corresponding to the area of the film and scaled proportionally as indicated in Fig. 1 and Eq. (6). The process allows a direct comparison of the image and the perspective projection of the DEM.
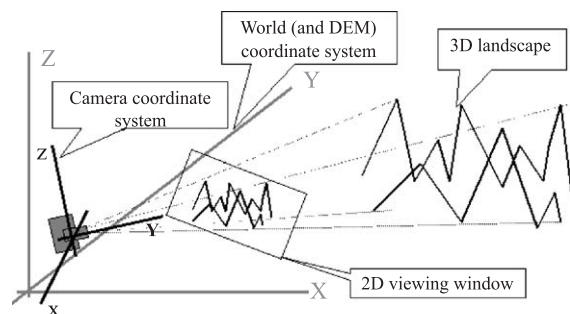

Fig. 1. Georeferencing process. The coordinates of the original 3D landscape are transformed to the camera referenced system and then projected onto a viewing window corresponding to the flat 2D camera film or CCD sensor.

If the result is satisfactory, the pixels in the image are allocated the *x,y,z* values of the corresponding grid cells in the DEM. The result is a georeferenced map of reflectance values shown in Fig. 2.

The viewing transformation, which rotates the translated coordinates according to the viewing reference system, is:

$$
\begin{pmatrix} P_{cx} \\ P_{cy} \\ P_{cz} \\ w \end{pmatrix} = \begin{pmatrix} U_x & U_y & U_z & 0 \\ V_x & V_y & V_z & 0 \\ N_x & N_y & N_z & 0 \\ 0 & 0 & 1/f & 1 \end{pmatrix} \begin{pmatrix} P_{tx} \\ P_{ty} \\ P_{tz} \\ 1 \end{pmatrix},
\tag{1}
$$

where *f* is the focal length of the lens, P_t is the translated point to a reference system with origin at *C*, the camera position (simply by adding the inverse of the camera coordinates to the original world coordinates), and P_c is the resulting coordinates of a point in camera coordinate system.
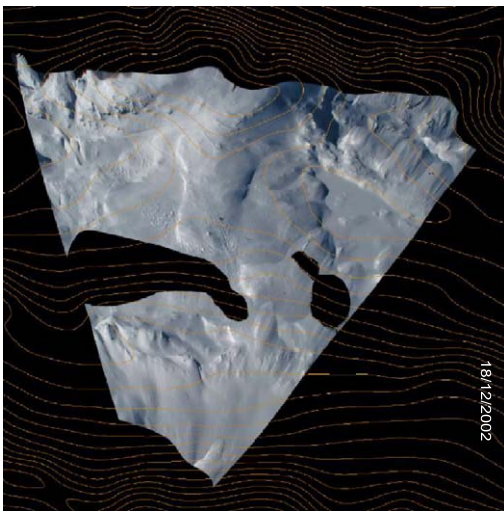

Fig. 2. Georeferenced map of reflactance values. Original image taken from Pic du lac Blanc, 3323 m asl. as shown in Fig. 4. The resolution of the image is 1 m. Note the mounds to the east and south of the Col du Lac Blanc (upper left side of the image) that corresponds to artificial snow mounds made for avalanche dog training.

The calculation of the unit vectors defining the viewing geometry is as follows. The viewing direction or vector $\vec{N}$ is:

$$
\vec{N_0} = T - C,
\tag{2}
$$

$$
\vec{N} = \frac{\vec{N_0}}{|\vec{N_0}|},
\tag{3}
$$

where *T* is the coordinate of the target (aim of the camera) and *C* is the coordinate of the camera with respect to the DEM origin of coordinates. From here, in a slightly modified manner than that of Fiume (1989) or Watt and Policarpo (1998), $\vec{U}$ and $\vec{V}$ are calculated using simple vector calculus, by finding the cross products:

$$
\vec{U} = \begin{cases} \vec{N} \times \dfrac{\vec{N_{xy}}}{|\vec{N_{xy}}|} & \text{if } N_z > 0 \\[2mm] \dfrac{\vec{N_{xy}}}{|\vec{N_{xy}}|} \times \vec{N} & \text{if } N_z < 0 \end{cases},
\tag{4}
$$

$$
\vec{V} = \vec{N} \times \vec{U},
\tag{5}
$$

where $\vec{N_{xy}}$ is the projection of $\vec{N}$ onto the horizontal plane, or $(N_x, N_y, 0)$, and N_z the *z* coordinate of vector $\vec{N}$. The resulting *x,y* coordinates of the final perspective projection, following Watt and Watt (1992), are calculated as:

$$
P_{px} = \frac{fP_{cx}}{\frac{1}{2}wP_{cz}} \quad \text{and} \quad P_{py} = \frac{fP_{cy}}{\frac{1}{2}wP_{cz}},
\tag{6}
$$

where $P_{p(x,y)}$ are the new *x,y* coordinates of the perspective projection of the point $P_{c(x,y,z)}$ onto the projection plane, which in this case is the film. The factor 1/2 is introduced in the denominator to set the origin of coordinates in the projection plane to the centre of the film, and *w* is calculated in Eq. (1).

In order to speed up the process, a first test is done using only a few ground control points (GCPs), instead of all the DEM grid cells. This permits correcting for errors and uncertainties in the correct position of the camera, target (central point of the image at which the camera points) and errors derived

from DEM discretisation of the real terrain and further interpolations. At present, GCPs were collected using a nondifferential global positioning system (GPS) without phase carrier, with a nominal precision of 15 m but an actual precision much lower, as could be realised by plotting the dispersion of values taken on different days at the same point. This might introduce large errors in the process that could be corrected using a differential GPS. Additional errors are derived from the use of nonmetric cameras and lenses which have an actual focal length different from that specified by the manufacturer and probably some degree of distortion in the resulting image. This last error is expected to be smaller than the original 45-m resolution of the DEM at which the model is run.

The final result of the georeferencing process is a georeferenced map of reflectance values (Fig. 2). From this map, any observable variation of the snow cover can be located with relative precision and associate to the outputs of the model. In this way, areas of erosion and deposition can be pinpointed, as well as areas of different albedos related to different histories of snow evolution and transport.

3.2. Relative albedo from photography

The light reflected from any point on the photographed area and recorded by the camera will depend both on the reflective properties of the surface (albedo) and on the incoming light falling on the surface. The illumination will depend on multiple parameters, such as the position of the sun, transmissivity of the atmosphere and reflected radiation from surrounding terrain. Thus, if these parameters are known, it is possible to derive the variations in reflectance due only to the variations of the albedo of the surface. A photographic camera can not give precise radiometric information. However, if we know the response of the photographic sensor, we can relate variations of pixel reflectance to albedo variations after correction for incoming illumination differences. The response of the sensor is usually linear within a range of exposure, becoming rapidly flat for both under and over exposed regions. This sensor response is estimated by photographing a greyscale card of known reflectance values, ranging from 5% to 95% reflectance. To estimate the relative albedo, we normalise the georeferenced reflectance

map according to incoming radiative fluxes, calculated according to:

$$I_i = rI_{sc}\tau_i(F_t + F_{sk} + F_{ms} + F_{sn}) \tag{7}$$

where I_{sc} is the solar constant or 1367 Wm^{-2}; r is the reciprocal of the square of the radius vector of the earth or correction for the eccentricity of the earth's orbit, calculated using Fourier series derived by Spencer (1971). The τ_i represents a set of atmospheric transmittance functions, both for diffuse and direct radiation. These functions take into account Rayleigh and Mie scattering in the standard composition of the atmosphere, transmittance by ozone, by water vapour and by aerosols, and are computed following a parametric model by Iqbal (1983). This model is one of the best performing ones in an intercomparison study carried out by Niemelä et al. (2001). The τ-functions incorporate the relative optical path length and pressure corrected air mass, depending on solar zenith angle and altitude. Additional updates to Iqbal's model are introduced for ozone layer thickness, which is taken from measurements of the NASA Total Ozone Mapping Spectrometer dataset (TOMS-EP, 2001), for the calculation of precipitable water, following Prata (1996), and for increased transmittance with altitude in accordance with values recommended by Bintanja (1996). The calculations of the F-terms are explained in detail by Corripio (in press); a similar approach is described by Greuell and Smeets (2001). These terms represent corrections for the angle of incidence of sun on the slope, corrected only for direct radiation; correction for diffuse radiation depending on the portion of the unobstructed upper hemisphere (skyview factor); diffuse radiation due to multiple scattering between the ground and the sky, incorporated in Iqbal's model and depending on the estimated general albedo of the area; and reflected radiation from surrounding slopes calculated as a function of horizon obstruction (1-skyview factor). The calculation of the sun vector, the vector normal to the surface and the skyview factor is explained by Corripio (2003). Additional corrections are made to account for the transmittance due to the intervening atmosphere between the camera and any reflecting surface recorded by the image. In the case of large horizontal distances, this last correction may be rather important, its value is calculated using the

atmospheric transmittance model MODTRAN (Berk et al., 1989).

The value of the reflected radiation arriving at every pixel of the camera will be:

$$R = I_i \alpha \Omega \tau_t. \tag{8}$$

From here we can derive the albedo as a reference to a pixel of known albedo, as the ratio of the reflectance of any given pixel R_n to a reference pixel reflectance R_{ref} corrected for the radiometric and geometric factors F indicated in Eq. (7). Omitting the product operator for the atmospheric transmittances, we have:

$$\alpha_n = \alpha_{ref} \frac{R_n}{R_{ref}} \frac{(\tau_i \tau_t) n (F)_{ref}}{R_{ref} (\tau_i \tau_t)_{ref} (F)_n}, \tag{9}$$

where (τ_i) and $(\tau_i)_{ref}$ may cancel each other if altitudinal variations within the area under consideration are small. A further simplification cancels the solid angle of view factor Ω, as all pixels in the camera are of equal size and similar field of view, thus, $\Omega_n = \Omega_{ref}$ is the near-horizontal atmospheric transmittance between the pixel position and the camera position which varies along the range of distances and altitudes of the DEM. Eq. (9) tell us that variations in pixel reflectance after corrections for differences in topographic configuration and thickness of intervening atmosphere between camera and observed pixel are due to differences in albedo of the corresponding pixel surface. Fig. 3a shows the results of this normalisation for an image of the Col du Lac Blanc taken on the 18th of February, 2003.

It should be noted that we are dealing with a camera designed to record light mostly in the visible band of the spectrum; however, most of the variation in snow albedo occurs in the near infrared (NIR; Wiscombe and Warren, 1980; Nolin and Dozier, 2000). The exact response of the camera in the NIR region is unfortunately unknown to us as the manufacturers classify it as confidential information. Nonetheless, tests with narrow band spectral filters show that the camera CCD is sensible to light at least up to 1050 nm, although the exact response curve is unknown. A rough estimation of the errors in the calculated albedo for this reason could be up to 4% or 5% for the worst scenario. This estimation is made using a radiative transfer model to calculate the
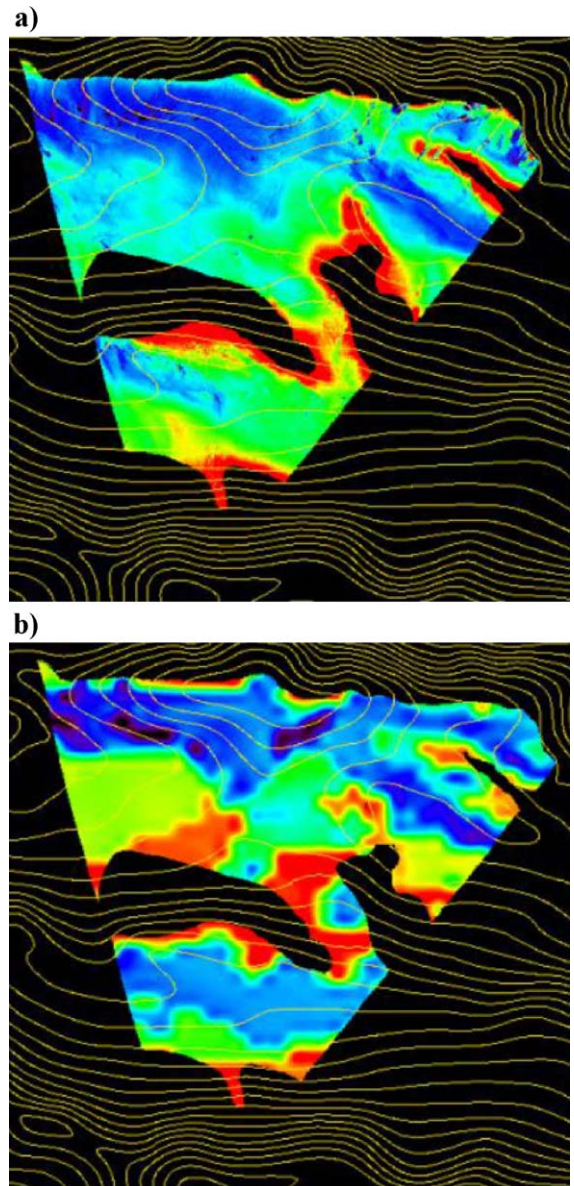

Fig. 3. Comparison between albedo derived from the photographic image (a) and albedo modelled according to snow grain types modelled by SYTRON2 (b). Colours are enhanced to show relative differences, with red higher and blue lower. North is right, as in Fig. 2. For interpretation of the references to colour in this figure legend, the reader is referred to the web version of this article.

energy per spectral band of incoming solar radiation and accounting for the uncertainties in the spectral latitude and response curve of the camera. The worst scenario implies dealing with the whole range of

snow types, from large round grains to dendritic fresh snow, which is not common in the winter months, except when radiative crusts are formed under intense solar radiation or at lower altitudes where there may be rain.

Additional corrections need to be performed to account for the anisotropic reflectance of the snow, especially as we are dealing with very oblique viewing angles. This is a complicated correction firstly because the anisotropy depends on the snow grain size and type and secondly because the subgrid topographic variations may play a very important role in the variation of surface reflectance. The safest approach is to mask out areas of very shallow illumination or viewing angles, following the arguably rule of thumb that albedo is independent of zenith illumination angle for angles smaller than $50°$ (Wiscombe and Warren, 1980). More recently, Warren et al. (1998) have published the results of their work on the anisotropy of Antarctic snow and sastruguis at shallow illumination angles, although for limited viewing angles. The incorporation of a correction following their recommended parameterisation is under consideration.

3.3. Modelled albedo

The output of the SYTRON2 model for validation purposes is a series of raster files with values for snow depth variation, snow grain characteristics (dendricity and sphericity) and snow grain sizes. The raster values contain a set of values for every grid cell in the DEM to which the model is applied. From these values, and following a process described by Brun et al. (1992) and based on Warren (1982) and Sergent et al. (1987), the albedo is derived as a function of optical grain size. In the visible band, the age of the snow (days since last snowfall) is also considered. Note that this parameter will be important under snowdrift conditions if a layer of older snow resurfaces due to wind erosion of upper layers. Thus, we have for the two bands in which our sensor is sensitive:

$$\alpha(0.3 - 0.8 \ \mu m) = 1 - 1.58 d^{\frac{1}{2}} - 0.2 \frac{\text{age}}{60} \qquad (10)$$

$$\alpha(0.8 - 1.15 \ \mu m) = 1 - 15.4 d^{\frac{1}{2}} \qquad (11)$$

where 0.2 is a site-dependant empirical coefficient and d is the optical grain size. It is worth noticing that

CROCUS is one of the best performing models regarding albedo estimation in a recent intercomparison study of snow models (Etchevers et al., in press).

3.4. Digital elevation model

Both the model and the georeferencing of terrestrial photography rely on the use of a high-resolution DEM and are limited by the accuracy of these data. For the present work, a digital elevation model at a resolution of 2 arc sec in latitude and 1.5 arc sec in longitude was purchased from the French Institut Géographique National (IGN). As the grid spacing is a constant angle of longitude in the X axis, this results in a north south gradient of the grid size. To simplify the use of the DEM and the georeferencing process, a regular squared grid at 45-m resolution was interpolated from the original DEM using bilinear interpolation. Additionally, to standardise the measurements with previous topographic surveys and the data collected by GPS, the original geographical coordinates in the WGS84 projection were transformed to the French system NTF Lambert III. For this procedure, we used the equations and the software CIRCE provided by the IGN (http://www.ign.fr).

To maximise the information extracted from the photographs, two additional DEMs were interpolated from the original, at resolutions of 5 and 1 m, respectively. This is done simply to map additional pixels in the photograph to locations within the original 45-m resolution grid cell. We know that the interpolated points at higher resolution are within the boundaries of a given original grid cell, but it is impossible to extract any relief information which was not contained in the original DEM at coarser resolution.

4. Results and discussion

Here we present the comparison of modelled and observed snow cover for two different situations, one with moderate to weak transport over a short period of time on the 18th of February, 2003, and the other after strong wind transport on the 5th of April, 2003.

Fig. 3a shows the relative albedo derived from a digital photography taken from the Pic du Lac Blanc,

3323 m asl. looking west to the Col du Lac Blanc, 2722 m. Fig. 3b is the albedo derived from SYTRON2 for the corresponding area. The triangular shape of the figure is due to the planar projection of the conical field of view of the camera. The camera was located on the highest contour seen at the bottom of the image, to the east, and the visible area is expanding with distance to the camera, hence the triangular shape. Black areas inside the coloured image are nonvisible areas, hidden behind cliffs or steeper slopes or masked out due to very low illumination or viewing angles. The narrow margins surrounding the borders of nonvisible areas in the sections closer to the camera, when they correspond to steep slopes, are at very shallow viewing angles, and the high albedo values should be considered carefully. The sun is slightly to the east at the time of taking the photograph. Thus, some of the areas approaching nonvisibility are also at very shallow illumination angles. Because the interception of direct solar radiation depends on relative local solar zenith angle, at very low angle, the correction of this value for the estimation of albedo is very sensitive to errors in both the ratio of direct to diffuse radiation and the amount of reflected radiation from surrounding slopes. However, areas approaching nonvisibility from the opposite side of the viewing point tend to be more perpendicular to both sun (at this time) and camera. Therefore, these values are more reliable. The colour table is stretched and contrasted to show the differences and the values are relative, with red higher and blue lower. The lower values on the upper left corner are due to the presence of bare rocks and to the orientation of the slope, almost perpendicular to the morning sun, which results in efficient interception of solar radiation and rapid metamorphism of the snow.

The meteorological conditions of the date when the image was acquired are characterised by moderate winds and low temperature with moderate snow transport in the previous hours. The model SYTRON2 is coupled with the model CROCUS (Brun et al., 1989, 1992), which provides the initial snow surface type. In this case, we had a thin radiative crust of lower albedo buried by new precipitation. Part of this crust resurfaced after the snowdrift event. This situation resulted in enhanced albedo variations, corresponding to areas of fresh angular snow and areas of larger grains highly metamorphosed. This situation was fortunate, as it allowed an enhanced contrast in the surface snow reflectance, both in the albedo derived by the models and in those obtained from the photographic image.

We restrict ourselves to a qualitative evaluation of the results until further refinements in the accuracy of the GCP and DEM resolution, and the appropriate corrections for the anisotropy of the reflected light by the snow. Under this restricted evaluation, we can say that the agreement between the figures, that is, photographically derived relative albedo and that derived from the modifications of the snow grains modelled by SYTRON2, is rather good. The main general patterns of higher and lower albedo coincide in both images. Areas where we could expect lower metamorphism of the snow and therefore higher albedo, such as shaded slopes or the steep slopes of Pic du Lac Blanc, in the bottom narrower section of the image, are well identified in both figures. The small lobe of higher albedo extending toward the SW from the center of the slope, visible in the photograph, but not in the model output, corresponds to enhanced scatter by the irregular snow surface of a small avalanche, an event SYTRON2 is not designed to recognise.

A different approach was used in Fig. 4, where an infared filter Kodak Wratten gelatin 87C was applied to the camera. This filter cuts out all light of wavelength shorter than 790 nm; thus, the image reveals the near infrared reflectance of the snow. Snow albedo variation is maximum in this region of the spectrum (Wiscombe and Warren, 1980; Nolin and Dozier, 2000), which enhances the contrast of the snow surface according to snow grain characteristics, as seen in Fig. 4. The darker areas, regularly on slopes facing north, are regions where snow has been eroded by the wind, exposing older snow underneath, and in most cases, a thin layer of radiative crust. This fact was verified by close inspection of the snow surface shortly after taking the picture. The difference is manifest when compared with the image in the visible band (Fig. 4), while the visible image (Fig. 4a) shows a uniform snow surface, the NIR image (Fig. 4b) shows patches of very contrasted snow surface, the darker areas corresponding to the resurfacing of crust after wind erosion. The pattern of erosion is consistent with the meteorological situation
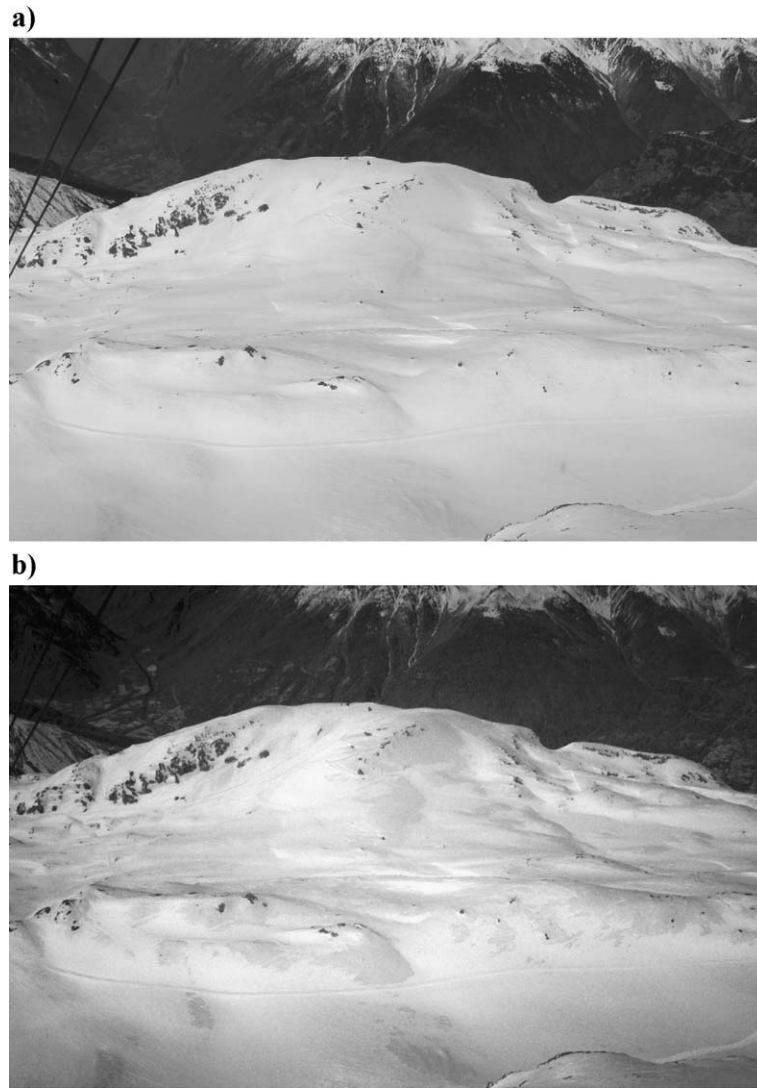
a)

b)

Fig. 4. Comparison between a photographic image in the whole visible plus NIR band (a) and an image taken with an infrared filter (b) that suppresses wavelengths shorter than 790 nm. Note the enhanced contrast due to different snow type (mainly radiative crust) on the NIR image, on the right side. Image taken from Pic du Lac Blanc, 3323 m asl. looking west.

on the previous hours, with moderate to intense northeasterly winds.

In order to relate the areas of erosion in the image to the output of the models, a manual classification of the picture was done into areas of erosion, deposition, likely erosion and likely deposition, using the NIR contrasted image and knowledge of the situation after direct observations on the test site. These areas are marked red, blue, orange and green, respectively, on the image and then georeferenced to the DEM (Fig. 5a). The result is compared to the output of SYTRON2 for accumulation and erosion areas (Fig. 5b). The largest accumulation areas coincide in both the manually mapped image and the model output. The upper part of the largest accumulation patch, toward the upper centre of the image, is probably realistic, but is not indicated in Fig. 5a as it corresponds to a ski slope,
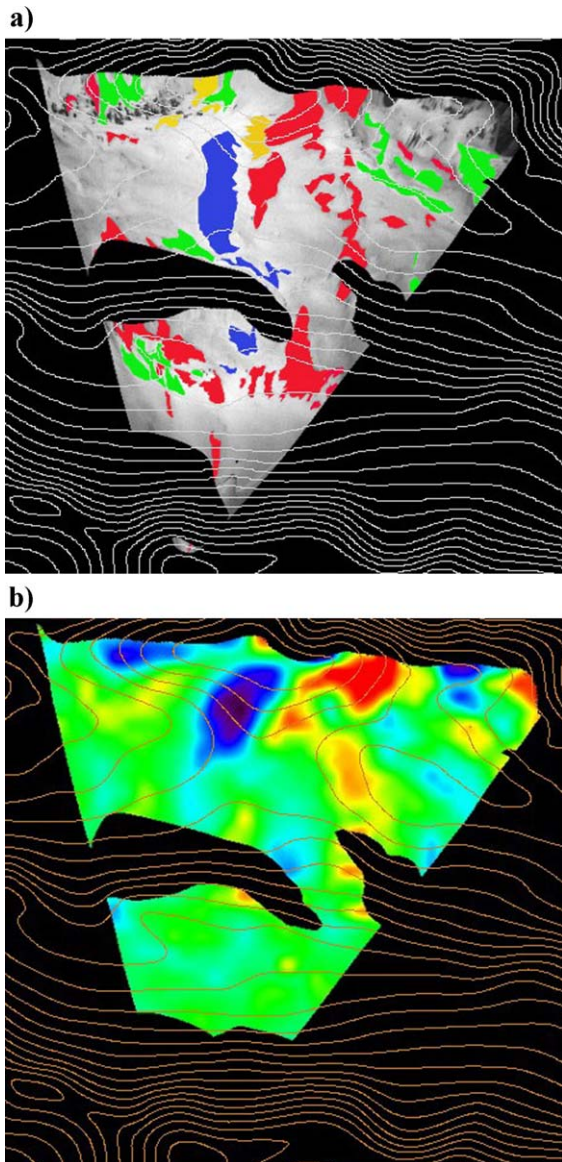
a)

b)

Fig. 5. Comparison between manually mapped areas of snow accumulation (blue and green) and erosion (red and orange; a) and those modelled by SYTRON2 at the Col du Lac Blac experimental site (b). Colours range from red (erosion) to blue (accumulation). North is right.

and the human disturbance is important. The largest areas of erosion also show a good agreement, with the exception of the cliffs on the upper left of the image. The cliffs are not well represented in the

DEM, although SYTRON2 includes the possibility of artificially introduced mask areas where accumulation or erosion is forbidden. New runs investigating the performance of the mask are under way. Areas of erosion clearly visible on the photograph but of surface smaller than 45×45 m are impossible to reproduce by the model, as this is the maximum resolution of the employed digital elevation model.

5. Limitations and future work

The most obvious limitation is the impossibility of modelling variations at a very small scale. The maximum resolution is determined not only by the available digital elevation model but also by the computational costs of diminishing the cell size and the uncertainties in the downscaling of the wind model at such a resolution. However, we can see from the images of the area that generally there is a considerable variation in snow texture, accumulation and erosion at subgrid scale. Nonetheless, the model allows the masking of areas such as small cliffs that may scape the resolution of the DEM but can be identified from the images or from local knowledge of the area of interest.

Future improvements of the model include the addition of multiple vertical layers and interaction between the layers, the improvement of the erosion/accumulation laws, improvements to the wind field and improvements in the temporal evolution of the snow, accounting better for the full thermodynamics of the snow surface during snowdrift events.

The monitoring technique would permit better accuracy when ground control points can be precisely located using either differential GPS or traditional topographical surveys. This is likely to be available in a recent future. Additional improvements can be derived from the application of corrections for the anisotropy in the reflection of the snow, especially at very shallow viewing angles. However, due to the effect of grain size on spatial distribution of the reflected radiation field, to the high values of this correction at very shallow angles, and due to the limitations of a simple recording device such as a digital camera, these corrections will always be limited.

6. Conclusion

We present an overview of the current efforts at CEN–Météo France in modelling wind and snowdrift over complex topography. We also introduce a novel technique for the spatial validation of the model, a technique which allows high temporal and spatial resolution. The approach is a land-based remote sensing tool based on recognising the optical variations on snow reflectivity and patterns that can be related to the corresponding effects of wind transport. At this stage, the qualitative comparison of modelled and measured outputs is satisfactory and reveals that the model is able to reproduce the general trends of snow erosion and accumulation at the scale of a few tens of metres. The results are even more satisfactory given the model constrains, as it is designed to be an operational model that needs to be run in real-time as an aid tool to avalanche hazard forecasting. There is room for improvement both in the modelling and in the monitoring approaches, and in this sense, the monitoring process is a useful tool to detect points in the model that can be improved.

Acknowledgements

References

Berk, A., Bernstein, L.S., Robertson, D.C., 1989. MODTRAN: a moderate resolution model for LOWTRAN 7. Technical Report GL-TR-89-012. Air Force Geophysics Laboratory, Hanscom Field, Massachusetts.

Bintanja, R., 1996. The parameterization of shortwave and long-wave radiative fluxes for use in zonally averaged climate models. Journal of Climate 9, 439–454.

Brun, E., Martin, E., Gendre, V.S.C., Coleou, C., 1989. An energy and mass model of snow cover suitable for operational avalanche forecasting. Journal of Glaciology 35 (121), 333–342.

Brun, E., David, P., Sudul, M., Brugnot, G., 1992. A numerical model to simulate snow cover stratigraphy for operational avalanche forecasting. Journal of Glaciology 38 (128), 13–22.

Corripio, J.G., 2003. Vectorial algebra algorithms for calculating terrain parameters from DEMs and the position of the sun for solar radiation modelling in mountainous terrain. International Journal of Geographical Information Science 17 (1), 1–23.

Corripio, J.G., 2004. Snow surface albedo estimation using terrestrial photography. International Journal of Remote Sensing (in press).

Durand, Y., Giraud, G., Mérindol, L., Martin, E., 1999. A computer-based system simulating snowpack structures as a tool for regional avalanche forecast. Journal of Glaciology 45 (151), 466–484.

Durand, Y., Guyomarc'h, G., Mérindol, L., Corripio, J.G., 2004. 2D numerical modelling of surface wind velocity and associated snow drift effects over complex mountainous orography. Annals of Glaciology 38 (in press).

Etchevers, P., Martin, E., Brown, R., Fierz, C., Lejeune, Y., Bazile, E., Boone, A., Dai, Y., Essery, R., Fernandez, A., Gusev, Y., Jordan, R., Koren, V., Kowalczyk, E., Nasonova, N.O., Pyles, R.D., Schlosser, A., Shmakin, A.B., Smirnova, T.G., Strasser, U., Verseghy, D., Yamazaki, T., Yang, Z., 2004. Intercomparison of the surface energy budget simulated by several snow models (SNOWMIP project). Annals of Glaciology 38 (in press).

Fiume, E.L., 1989. The Mathematical Structure of Raster Graphics. Academic Press, Boston.

Föhn, P.M.B., Meister, R., 1983. Distribution of snow drifts on ridge slopes: measurements and theoretical approximation. Annals of Glaciology 4, 52–57.

Foley, J.D., van Dam, A., Feiner, S.K., Hughes, J.F., 1990. Computer Graphics, Principles and Practice Addison-Wesley, Reading, MA.

Gauer, P., 1998. Blowing and drifting snow in alpine terrain: numerical simulation and related field measurements. Annals of Glaciology 26, 174–178.

Greuell, W., Smeets, P., 2001. Variations with elevation in the surface energy balance on the Pasterze, Austria. Journal of Geophysical Research 106 (D23), 31,717–31,727.

Guyomarc'h, G., Mérindol, L., 1991. Etude du transport de la neige par le vent. Actes du Syposium CISA-IKAR, Chamonix, 4–8 June 1991, ANENA, Grenoble. ANENA, Grenoble, France, pp. 77–82.

Guyomarc'h, G., Mérindol, L., 1995. Vers une prevision locale du transport de neige par le vent. In: Sivardiére, F. (Ed.), Les apports de la recherché scientifique à la sécurité de la neige, glace et avalanche. Actes du colloque, Chamonix, 30/05–3/06 1995. ANENA, Grenoble, pp. 97–102.

Holton, J.R., 1979. An Introduction to Dynamic Meteorology, 2nd ed. Academic Press, Orlando.

Iqbal, M., 1983. An Introduction to Solar Radiation. Academic Press, Toronto.

Lehning, M., Doorsschot, J., Fierz, C., Radersschall, N., 2002. A 3D model for snow drift and snow cover development in steep alpine terrain. In: Stevens, J.P. (Ed.), International Snow Science

Workshop Proceedings, ISSW'2002, Penticton, British Columbia, 29 September–4 October 2002. Electronic publication, Penticton, BC.

Liston, G.E., Sturm, M., 1998. A snow-transport model for complex terrain. Journal of Glaciology 44 (148), 498–516.

Mellor, M., 1965. Blowing Snow, Vol. III-A3c. Hanover, New Hampshire, USA.

Niemelä, S., Räisänen, P., Savijärvi, H., 2001. Comparison of surface radiative flux parameterizations: Part II. Shortwave radiation. Atmospheric Research 58, 141–154.

Nolin, A.W., Dozier, J., 2000. A hyperspectral method for remotely sensing the grain size of snow. Remote Sensing of Environment 74, 207–216.

Pomeroy, J.W., Gray, D.M., 1995. Snowcover: accumulation, relocation and management, National Hydrology Research Institute, University of Saskatchewan, Saskatoon, 144 pp. (NHRI Science Report 7).

Prata, A.J., 1996. A new long-wave formula for estimating downward clear-sky radiation at the surface. Quarterly Journal of the Royal Meteorological Society 122, 1127–1151.

Purves, R.S., Barton, J.S., Mackaness, W.A., Sugden, D.E., 1998. The development of a rule-based spatial model of wind transport and deposition of snow. Annals of Glaciology 26, 197–202.

Ryan, B.C., 1977. A mathematical model for diagnosis and prediction of surface winds in mountainous terrain. Journal of Applied Meteorology 16 (6), 571–584.

Sergent, C., Chevrand, P., Lafeuille, J., Marbouty, D., 1987. Caractérisation optique de différents types de neige. extinction de la lumière dans la neige. Journal de Physique 48 (Colloq C1.), 361–367 (Supplement au 3. Paris).

Spencer, J.W., 1971. Fourier series representation of the position of the sun. Search 2, 172.

Takeuchi, M., 1980. Vertical profile and horizontal increase of drift-snow transport. Journal of Glaciology 26 (94), 481–492.

TOMS-EP: 2001, Total Ozone Mapping Spectrometer–Earth Probe data sets. http://toms.gsfc.nasa.gov/eptoms/ep.html.

Warren, S.G., 1982. Optical properties of snow. Reviews of Geophysics and Space Physics 20 (1), 67–89.

Warren, S.G., Brandt, R.E., Hinton, P.O., 1998. Effect of surface roughness on bidirectional reflectance of Antarctic snow. Journal of Geophysical Research 103 (E11), 25789–25807.

Watt, A.H., Policarpo, F., 1998. The Computer Image Addison-Wesley, Harlow.

Watt, A.H., Watt, M., 1992. Advanced Animation and Rendering Techniques: Theory and Practice, ACM Press, Addison–Wesley, New York.

Wiscombe, W.J., Warren, S.G., 1980. A model for the spectral albedo of snow: I. Pure snow. Journal of the Atmospheric Sciences 37, 2712–2733.